Islet Amyloid: Phase Partitioning and Secondary Nucleation Are Central to the Mechanism of Fibrillogenesis†

Shae B. Padrick and Andrew D. Miranker*

Department of Molecular Biophysics and Biochemistry, Yale University, 260 Whitney Avenue, New Haven, Connecticut 06520-8114

Received December 14, 2001; Revised Manuscript Received January 28, 2002

ABSTRACT: Islet amyloid polypeptide (IAPP) contributes to the pathogenesis of type II diabetes by depositing as cytotoxic amyloid fibers in the endocrine pancreas. Fiber formation occurs with a marked conformational change from an unstructured precursor. Using real-time quantitative kinetic methods, fibrillogenesis was characterized as a function of protein, denaturant, and seed concentration. Several observations are in sharp contrast to the expectations for nucleation-dependent polymerization. First, the half-time of conversion for both *de novo* and seeded kinetics were found to be independent of protein concentration. Second, while elongation kinetics scale linearly with protein concentration, they are relatively insensitive to changes in the total seed concentration. Third, seeded bypass of *de novo* fiber formation kinetics shows a lag phase. The seeded lag phase is eliminated by a time delay before the introduction of seed to a *de novo* reaction. Last, conversion is highly cooperative, with the time required for 10−90% conversion occurring much faster than the lag time. At a minimum, four kinetic steps are required to describe these observations: activation, fiber independent nucleation, fiber-dependent nucleation, and elongation. Furthermore, we invoke a phase transition in which protein initially forms an off-pathway dispersion. This single construct allows us to model both the concentration independence of the *de novo* reaction time and the first-order concentration dependence of the elongation kinetics. Marked acceleration of this reaction by hexafluoro-2-propanol reinforces this view by altering the relative solubility of the two phases and/or by stabilizing hydrogen-bonded structures in the transition states of the reaction pathway.

Formation of amyloid plaques is a unifying feature of the pathology of a range of diseases, including Alzheimer's, Huntington's, and Parkinson's (*1*). Proteinaceous fibers are a central component of these plaques and are typically composed of linear, unbranched, and noncovalent aggregates of a single polypeptide chain. In dialysis-related amyloidosis, for example, the polypeptide is β-2 microglobulin (β2m) from class I MHC (*2*). In type II diabetes, the polypeptide is islet amyloid polypeptide (IAPP)[1] (*3*, *4*). In each case, the protein undergoes a conformational change and deposits with characteristic pathology. β2m gives rise, predominantly, to deposits in the joints, while IAPP deposits form in the endocrine pancreas. While amyloid fibers are derived from precursors with distinct primary and tertiary structures, the resultant fibers share a number of characteristics. These include a crossed-β sheet organization in which the β strands are arranged perpendicular to the fiber axis, resistance to proteolysis, and the display of birefringence upon binding of the histological dye, Congo red (*5*).

The kinetics of fiber formation are particularly fascinating as they are nucleation-dependent (*6*). Fiber formation reactions are generally characterized by a lag phase in which no detectable fibers are formed. This is then followed by an explosive elongation phase in which fiber is formed over a period of time which is often shorter than the lag phase itself. The lag phase is circumvented by providing preformed fibers as seed to a *de novo* reaction. Amyloid fibers have generally been found to seed only reactions containing the precursor from which they were formed. This indicates that although the secondary and ultrastructure of different amyloids are similar, there must be specificity at the level of tertiary or quaternary structure. A particularly clear example is the inability of Aβ fibers formed from D-amino acids to seed L-Aβ precursor (and vice versa) (*7*). Recently, cross seeding kinetic behavior of closely related prion sequences from *S. cerevisiae* and *C. albicans* has been used to describe a mechanism for species barrier crossing by prions (*8*). Such studies strongly suggest that, despite ultrastructural and histological commonalities, there exists a specific and defined structure to fibrillar aggregates.

IAPP is a 37-residue peptide hormone that is cosecreted with insulin by the β cells of the pancreas. Deposition of unmodified IAPP as amyloid fibers is observed in greater than 90% of type II diabetics (*4*). As IAPP is cytotoxic to cultured β cells, deposition is likely to be causal to the

† Supported by a grant from the National Institutes of Health (DK54899). S.B.P. is supported by a National Science Foundation Graduate Research Fellowship. A.D.M. is a Pew Scholar in the biomedical sciences.

* To whom correspondence should be addressed. Phone: (203) 432-8954. Fax: (203) 432−5175. E-mail: Andrew.Miranker@yale.edu.

[1] Abbreviations: Aβ, amyloid β peptide associated with Alzheimer's disease; CD, circular dichroism; DNM, double-nucleation mechanism; HbS, hemoglobin S; HFIP, 1,1,1,3,3,3-hexafluoro-2-propanol; IAPP, islet amyloid polypeptide; NCC, nucleated conformational conversion; NDP, nucleation-dependent polymerization; NM, N-terminal and middle domains of Sup35 from *S. cerevisiae;* PMF, phase-mediated fibrillogenesis; TEM, transmission electron microscopy; ThT, thioflavin T.

10.1021/bi0160462 CCC: $22.00 © 2002 American Chemical Society
Published on Web 03/12/2002

observation of β cell depletion in type II diabetics (*9*). Systemic insulin resistance in these patients leads to abnormally elevated secretion of insulin and IAPP (*10*). In the context of any nucleation-dependent polymerization model, it is reasonable to assert that fiber formation by IAPP is a consequence of raised local concentrations of polypeptide. However, the concentration of IAPP in the secretory granule is ~400 μM (*11*). As full-length IAPP can readily be converted to amyloid at concentrations which are 2 orders of magnitude lower (*12*, *13*), increased secretion may be necessary but is not a sufficient explanation for *in vivo* deposition.

To understand the process by which IAPP converts to a defined fibrillar structure, a detailed determination of the kinetics and structures of intermediate states along the pathway is necessary. This is analogous to the study of protein folding and is particularly challenging as a consequence of the oligomeric and heterogeneous nature of fiber assembly. Recently, we characterized the intrinsic fluorescence of IAPP during lag and end phases under near-physiological conditions (*12*). The fluorescence of IAPP is dominated by a single C-terminal tyrosine residue, Y37. Although this residue is outside the proposed amyloidogenic core (*14*) derived from peptide studies, it has several properties which indicate that it is critical to assembly and stability of full-length IAPP. First, it is near in space to F15 and F23 in both lag phase and fibrillar states. For the lag phase, this observation indicates a more condensed structure than the monomeric random coil conformation inferred from CD. Second, the pK_a of the tyrosine hydroxyl is shifted by ~2 pH units in the fibrillar state. Last, Y37 in fibrillar IAPP is buried and rigid to an extent comparable to that of free tyrosine in frozen solution.

In this work, we have capitalized on this final observation, the change in fluorescence anisotropy of tyrosine 37, to monitor fiber formation kinetics. Anisotropy is detected in real time, with high signal-to-noise, and on a timescale which is rapid as compared to fibrillogenesis. As the source of anisotropy is a single residue, we can relate our observations to a specific location within the primary structure of IAPP. Furthermore, anisotropy can be related directly to the formation of soluble IAPP which has been incorporated into fiber. Thus, anisotropy enables us to make quantitative, reproducible, and structurally assignable determination of the reaction pathway of IAPP fibrillogenesis.

MATERIAL AND METHODS

Peptides and Chemicals. HFIP was obtained from Sigma-Aldrich (Milwaukee, WI) and repurified by fractional distillation. Salts and buffers were obtained from J. T. Baker (Phillipsburg, NJ). Thioflavin T was purchased from Acros (Geel, Belgium). Human IAPP was synthesized by standard t-Boc solid-phase synthesis methods and purified in-house. Stock solutions of IAPP were prepared by solubilizing reversed-phase purified lyophilized peptide in 6 M guanidine HCl, 50 mM potassium phosphate (pH 6.0), and loading onto C18 reversed-phase spin column (Amica). After being washed first with 10% acetonitrile and 0.2% trifluoroacetic acid, followed by a water wash, peptide was eluted with 100% HFIP. Stock solution may contain residual water (<5%) but is treated as 100% for the purposes of calculating HFIP concentrations. The peptide concentration was determined by UV absorbance at 280 nm in 6 M guanidine HCl and 50 mM potassium phosphate (pH 6.0), using an extinction coefficient of 1400 M^{-1} cm^{-1}.

Production of Fibers. IAPP fiber formation was initiated by dilution of IAPP stock solution into standard reaction buffer 100 mM KCl and 50 mM K_2HPO_4/KH_2PO_4 (pH 7.4) at 25 °C. For experiments at different concentrations of protein, HFIP concentration was matched at 2.5% by the addition of HFIP to the reaction mixture prior to the addition of IAPP. For experiments varying the method of seed addition and varying the concentration of seed, HFIP was similarly maintained at 2%. Fiber used for seed was produced by diluting IAPP stock to 50 μM IAPP in reaction buffer at 5% (v/v) HFIP. The solution was incubated for 10 min at room temperature and fiber formation confirmed using Thioflavin T (*15*). Seed stock was then diluted 2-fold with a reaction buffer and briefly vortexed prior to each use. Seed age was kept at <8 h to ensure reproducibility.

Electron Microscopy. Carbon-coated copper grids were freshly prepared in-house and glow-discharged for 30 s immediately prior to use. Three microliters of 5 μM (monomer units) of a fiber solution was placed on prepared grids and incubated for 2 min. Grids were stained with 3 μL of 1% phosphotungstic acid (pH 7.6) for 1 min. Images were taken using a Phillips Technai 12 operating at 120 kV accelerating voltage. Images were collected using a 1000 × 1000 pixel Gatan 794 slow scan CCD at 11 000*x* magnification and 10 μm underfocus.

Circular Dichroism. Circular dichroism spectrum was measured on an Aviv 62DS spectrometer (Aviv Associates, Lakewood, NJ). Fibers were produced as the seed fibers were and diluted to 10 μM in IAPP concentration (in monomer units) for measurement. Measurement occurred at 100 mM KCl, 50 mM K_2HPO_4/KH_2PO_4 buffer (pH 7.4), and 2.5% HFIP at 25 °C. Measurements occurred every 1 nm with a 10 s averaging time per point in a quartz cell of 0.2 cm pathlength.

Fluorescence. All fluorescence experiments were performed on a PTI QuantaMaster C-61 2 channel fluorescence spectrophotometer fitted with a temperature-controlled cell holder and automated excitation shutter. Glan−Thompson style plane polarizers and G-factor corrections were used to calculate tyrosine anisotropy (*16*). Excitation was accomplished with a 5 nm slit width centered at 278 nm and detection by a 5 nm slit width centered at 303 nm. A total of 160 μL of 200 μL reactions were transferred into a 3 mm × 3 mm cuvette (Helma) and placed into cell holder. Dead times were 30−90 s for *de novo* experiments and 60−120 s for seeded experiments. ThT assays were performed by diluting fiber solutions to 0.5−1.0 μM fiber (in monomer units) in a ThT buffer. The ThT buffer is 5 μM ThT filtered at 0.2 μm with 50 mM glycine at pH 9.0. Fluorescence was measured without polarizers fitted and as an excitation spectrum scanning every 1 nm from 300−460 nm, detecting at 484 nm and averaging for 5 s at each point. Slit widths and cell were identical to those used in the tyrosine anisotropy measurements.

Data Analysis. Unless otherwise stated, anisotropy as a function of time, $r(t)$, was fit to a sigmoidal transition between two independent straight lines

$$r(t) = (m_1 \times t + r_1)\,\alpha + (m_2 \times t + r_2)(1 - \alpha)$$

where $\alpha = (1 + e^{((t_{50} - t)/\tau)})^{-1}$.

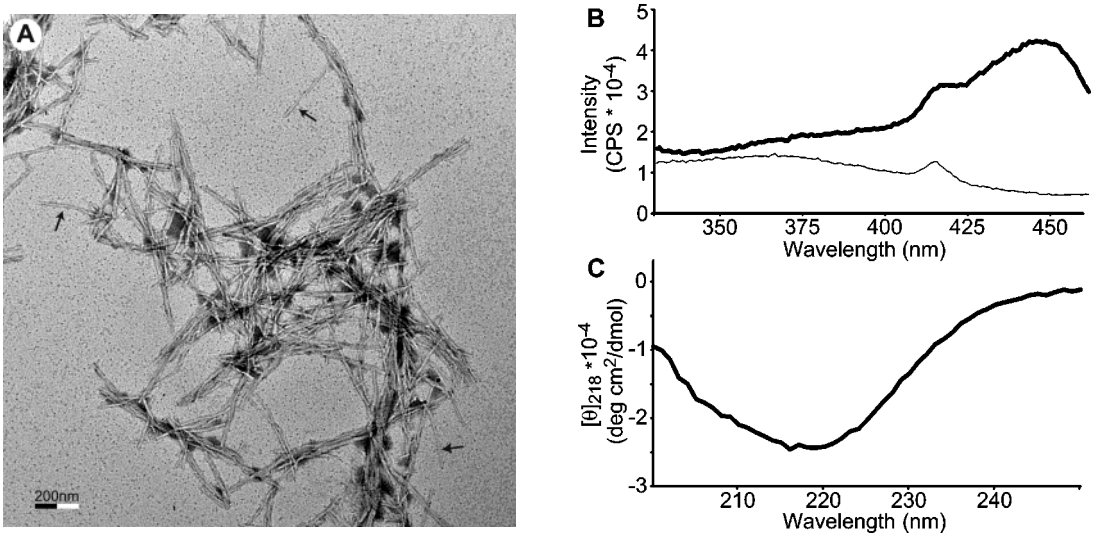

FIGURE 1: IAPP forms amyloid fibers. (A) Negative stain transmission electron micrograph of IAPP fibers generated at 5 μM of IAPP under our standard conditions. IAPP forms long unbranched fibers, consistent with typical amyloid morphology, that aggregate into large fiber masses. Several well-resolved fibers are indicated with arrows and were used to determine an average fiber width of ~12 nm. (B) IAPP fibers enhance the fluorescence excitation of the histological dye ThT. Fluorescence excitation spectra of 5 μM ThT in the presence (thick line) and absence (thin line) of 1 μM IAPP amyloid fibers. Fluorescence emission is detected at 484 nm. The excitation enhancement at 430−460 nm is characteristic of amyloid fibers (*15*). The small peak at 416 nm is from Raman scatter of water. (C) IAPP fibers are rich in β-strand secondary structure. A far UV CD spectrum of IAPP fibers shows a minimum near 218 nm, characteristic of a β-sheet.

Fitting was performed using the NonlinearRegress function in Mathematica 4.0 (Wolfram Research, Inc., Champaign, IL). Of the six parameters determined by the fit, two are presented routinely in this work: t_{50}, the center of the transition, and τ, the time constant of the transition. t_{50} is used without further modification, while τ is converted to a molar reaction velocity, $\nu_{t_{50}}$, at t_{50}. Upon renormalization of the fits (i.e., setting the baselines to 0 and 1), $\nu_{t_{50}}$ is computed as $\nu_{t_{50}} = [\mathrm{IAPP}]_{t=0}/(4\tau)$. Reported values of t_{50} and $\nu_{t_{50}}$ represent averages of at least three independent kinetic runs. Errors are quoted as one standard error of the mean.

Simulations. Simulated kinetic profiles are generated using finite difference methods (*17*, *18*). Briefly, rate laws for each kinetic step are used to numerically estimate the change in the populations of free monomer, fiber mass, and fiber ends over a time interval. A time interval on the order of $t_{50}/10000$ was sufficient for the integrations to converge. Nuclei size for NDP kinetics was chosen to be a trimer, although choice of other parameters has little impact on curve shape (*19*). Curves generated are indistinguishable from that reported for NDP. Generalized DNM kinetics similarly behaved as expected. In this work, a simulation is shown based on the double-nucleation model suggested for HbS (*20*), with homogeneous and heterogeneous nuclei sizes modeled as trimeric. Rate constants were chosen to give a curve that closely matched the shape of the IAPP data.

RESULTS

Fiber formation reactions are initiated by dilution of a stock solution of IAPP in HFIP into reaction buffer at pH 7.4 and 25 °C and ionic strength isotonic with serum. In HFIP, IAPP is indefinitely stable and does not give rise to fibers until it is diluted into aqueous media. Rather than solubilizing IAPP directly into HFIP, our stock solutions are prepared by eluting IAPP directly off of a reversed-phase column with 100% HFIP. Fibers are retained on the column under these conditions (data not shown). This eliminates stock-to-stock variations that we believe derive from fiber seed formation by IAPP in the lyophilized state. Kinetics of IAPP fiber formation are monitored by fluorescence anisotropy of the intrinsic tyrosine at residue 37. Fiber formation results in the burial of this residue into a rigid environment, comparable to that of a frozen solid (*12*). Furthermore, we have shown that the change in this observable correlates with the change in the ability of the protein to bind the amyloid-indicative histological dye, ThT. Thus, the change in anisotropy directly reflects amyloid fiber formation. Anisotropy, however, is measured in real time directly from a reacting sample rather than after the removal and quenching of discrete aliquots.

Fiber prepared over the range of conditions used here results in fiber properties which are consistent with previous reports (*21*). Observed by electron microscopy (Figure 1A), the fibers are long, straight, and unbranched, with a width of 11−14 nm, consistent with a predominant population of fibers composed of coiled 8 nm fibers (*21*). Fluorescence analysis of the fibers in the presence of ThT yields strong enhancement at the excitation wavelength of 460 nm (Figure 1B), which is widely attributed to the binding of ThT by amyloid fibers (*15*). Furthermore, analysis of secondary structure content using circular dichroism reveals the presence of structures which are rich in β-sheet conformations (Figure 1C), consistent with the cross β nature of amyloid fibers (*5*).

The fibrillogenesis kinetics of IAPP reveal two properties consistent with nucleation-dependent polymerization (*22*). First, fibers form spontaneously from a solution of precursor after a period of incubation with minimal signal change. Second, this period of time with little signal change can be bypassed by the addition of exogenous fiber. The first property, or *de novo* fiber formation, is demonstrated by the dilution of a 2 mM stock solution of IAPP to a concentration of 20 μM in a reaction buffer (Figure 2A). In this representative reaction, the lag phase is ~1600 s, and the transition to mature fibers takes ~400 s. The second property is demon-

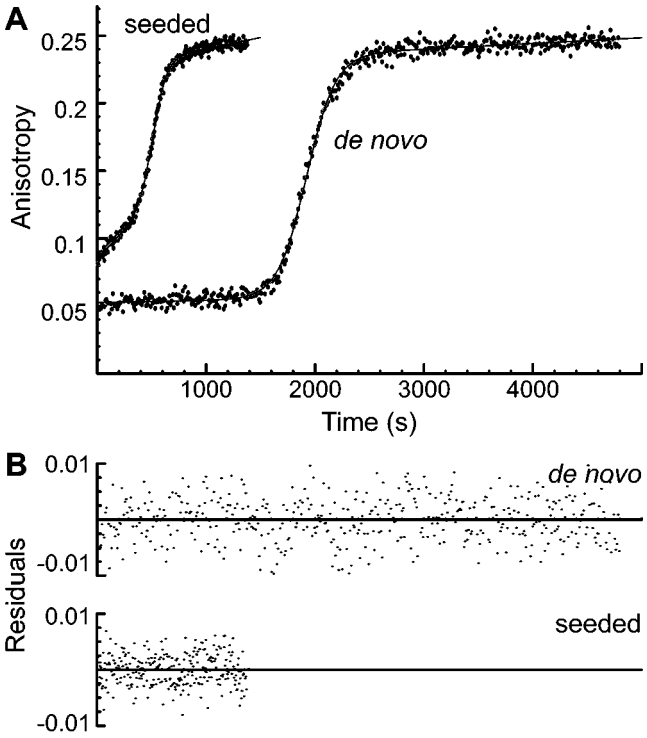

FIGURE 2: IAPP forms *de novo* fibers following a lag phase, which is completely bypassed by seeding. Fiber formation is monitored by fluorescence anisotropy, which shows the adoption of a rigid environment surrounding the intrinsic tyrosine. *De novo* and seeded curves are shown and annotated in the figure (A). Raw data is shown along with a fit to a six parameter sigmoid transition. Residuals of these fits (B) are small (<5%) and random. *De novo* kinetics are collected at 1 point/10 s, and seeded kinetics are collected at 1 point/5 s. Seeding was accomplished by adding 5% (by mass) of standard seed to an otherwise identical reaction.

strated by a reaction that is otherwise identical to the first except for the addition of 1 μM of preformed fibers (in monomer units). The seeded reaction reaches completion in less than 1000 s (Figure 2A). This is clearly shorter than the lag phase of the spontaneous reaction (i.e., *de novo* fiber formation has been completely bypassed). Consistency in seeded reactions is achieved by using freshly generated seed fibers following a standard protocol (see Materials and Methods).

Objective comparison of fibrillogenesis reactions requires a means of parameterization that is empirical and independent of a mass action model. We have found that both *de novo* and seeded fibrillogenesis of IAPP are well-described by a symmetric sigmoidal transition between two independent straight lines. This is a six parameter fit similar in form to that used for fitting equilibrium protein denaturation data (*23*). Residuals of these fits are random (Figure 2B), with a standard deviation of less than 5% the magnitude of the total change in anisotropy. Two objective parameters from the fits are considered routinely in this study. The first, t_{50}, is the time required for 50% conversion of material to fibrillar form. For the *de novo* and seeded reactions shown in Figure 2, these values are 1900 and 520 s, respectively. The second parameter, $\nu_{t_{50}}$, is the reaction velocity in monomer units at t_{50}. Detection of IAPP residual concentration, using a sensitive mass spectrometry-based assay (*24*), shows that IAPP is nearly completely consumed (>90%) in both *de novo* and seeded reactions (data not shown). Furthermore, the near-limiting anisotropy requires that the vast majority of IAPP be in the fibrous conformation (*12*). Additionally, under the conditions examined here, IAPP fluorescence intensity varies by less than 20% (data not shown). Therefore, we can determine $\nu_{t_{50}}$ from fits to the kinetic profiles (see Materials and Methods). These values are 38 and 79 nM/s, respectively.

Nucleation-dependent polymerization predicts that the length of the lag phase, measured by the characteristic time, t_{50}, will scale in inverse proportion to $[\text{precursor}]_0^{n/2}$, where n is the oligomeric size of the nucleus of fiber formation (*25*). To test this, we measured *de novo* fiber formation kinetics of IAPP over a 10-fold concentration range. Rather than demonstrating the predicted sensitivity to concentration, reactions at 5 and 50 μM have no apparent difference in t_{50} (Figure 3A). Objective measure of t_{50} for these reactions (Figure 3A, inset) yields an average, including all concentrations, of $t_{50} = 2100 \pm 450$ s. The value of t_{50} at each individual concentration is within the error of the overall average behavior. Because anisotropy is inherently concentration-renormalized and the curves at all concentrations are roughly superimposable, $\nu_{t_{50}}$ is roughly linearly proportional to protein concentration (Figure 3B). At concentrations of up to 30 μM, a linear dependence is observed with a slope of 2.1 ± 0.4 nM s^{-1} μM^{-1} and which extrapolates to near zero nM/s (0.4 ± 7) at zero concentration IAPP. Comparable studies, using far UV CD and light scattering, give similar results (data not shown).

IAPP kinetic profiles show the presence of an inflection point, even under seeded conditions (Figure 2A). This is an unexpected observation, as seeded reactions are expected to follow an exponential decay. This can be explained by only a limited number of possibilities. First, soluble IAPP may undergo conformational changes or oligomerization steps before becoming competent to elongate fibers. Second, seed held at high concentration and then diluted into a fresh reaction may take time to undergo conformational changes necessary for it to act as an effective seed. Last, it is possible that exogenous seed catalyzes the formation of new fibers. Upon being formed, these fibers as well as exogenous seed are elongated by soluble IAPP. We address these possibilities in turn.

First, consider the possibility that changes in IAPP are a prerequisite of elongation. This was tested by comparing the addition of seed at $t = 0$ (Figure 4, curve A) with the addition of seed at $t = 1800$ s (Figure 4, curve B) to a reaction whose *de novo* counterpart has a t_{50} of > 7200 s. Remarkably, the introduction of a delay prior to the addition of seed causes the inflection point to vanish. Fiber formation occurs immediately upon the addition of seed, resulting in a kinetic profile that fits to a single-exponential decay (fit not shown). The $\nu_{t_{50}}$ of the reaction seeded at $t = 0$ (curve A) is 10 ± 1 nM/s, which is comparable to the initial reaction rate, 14 ± 2 nM/s, for the reaction with a 30 min delay prior to seeding (curve B). These are the maximum observed fibrillogenesis rates for the two reactions. Their similarity suggests that the reactions are identical with respect to the elongation phase of the process. With preincubation times shorter than 20 min, kinetics containing an inflection point are observed but diminished in length (data not shown). Clearly, there is a pre-elongation step required in the assembly of IAPP.

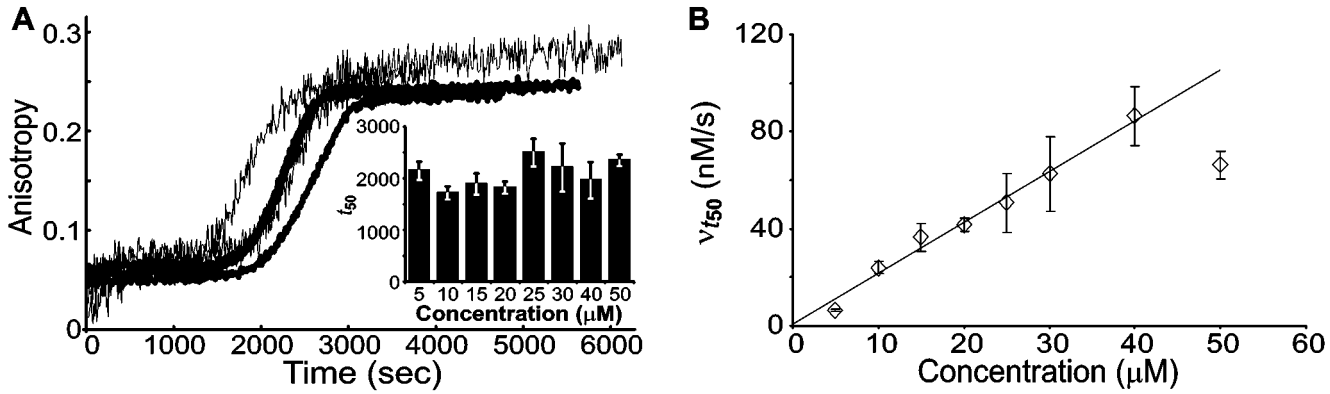

FIGURE 3: Protein concentration dependence of IAPP fibrillogenesis reactions. (A) Six representative kinetic profiles for fiber formation reactions at initial IAPP concentrations of 5 μM (thin lines) and 50 μM (thick lines). (A, inset) Average values of t_{50} for initial IAPP concentrations of 5−50 μM. (B) $\nu_{t_{50}}$ as a function of initial protein concentrations used in the reaction. A linear fit ($R^2 = 0.97$) to t_{50} (average values) at protein concentrations through 30 μM is shown. Reactions were performed by dilution of a stock solution of IAPP in HFIP into 100 mM KCl and 50 mM K_2HPO_4/KH_2PO_4 (pH 7.4) at 25 °C. HFIP was maintained at 2.5% in all reactions by the appropriate addition of HFIP to the reaction media.

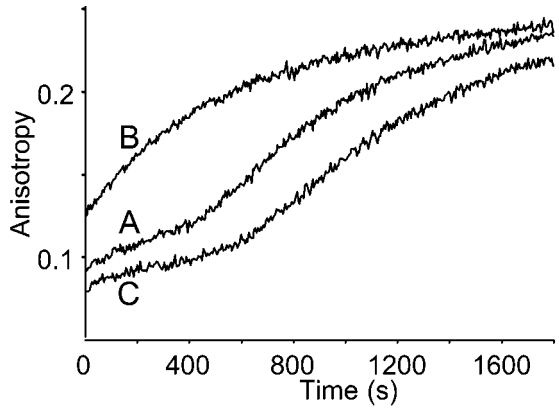

FIGURE 4: Determination of the effects of time on seeding of IAPP reaction. All reactions are at 10 μM IAPP, seeded with 1 μM IAPP fibers. Seeding immediately after the addition of soluble IAPP results in a kinetic profile that contains an inflection point (curve A). By contrast, when soluble IAPP is added first and incubated for 30 min prior to addition of seed, the inflection point in the seeded kinetics is lost (curve B). Adding the seed to the reaction buffer and waiting 30 min prior to adding soluble IAPP has little effect on the kinetic profile (curve C). Note that all reactions are completed on a timescale which is faster than the reactions unseeded counterpart (Figure 3). Profiles shown are averages of three repeats.

The pre-elongation step in seeded polymerization may require assembly of an oligomer. This was investigated and discounted by measuring the concentration dependence of the kinetics of seeded reactions at constant seed and varying soluble IAPP from 5 to 50 μM. Seed was added immediately following dilution of the IAPP stock, as in Figure 4, curve A. Representative reactions at 5 and 50 μM reveal qualitatively similar lengths of the lag phase and width of the transitions (Figure 5A). A quantitative assessment of t_{50} shows an average lag time of 560 ± 80 s with little variation (Figure 5A, inset). If oligomerization is involved in the pre-elongation step, the change in concentration should have yielded longer t_{50} at 5 μM soluble IAPP and shorter t_{50} at 50 μM. Qualitatively, higher concentrations of IAPP should more closely resemble curve B in Figure 4. Examination of $\nu_{t_{50}}$ as a function of concentration reveals that, at constant seed concentration, the rate of fiber formation varies linearly with IAPP concentration (Figure 5B). A line fit using points through 30 μM IAPP ($R^2 = 0.98$) yields a slope of 4.1 ± 0.2 nM s^{-1} μM^{-1}. At higher concentrations, the $\nu_{t_{50}}$ falls below the extrapolated line, suggestive of saturation of the reaction. Linear behavior is consistent with first-order kinetics, for example, rate laws of the form k[soluble IAPP][fiber ends].

Second, consider the possibility that seed itself must be activated following dilution. This was addressed by first diluting the exogenous seed into reaction buffer. This solution was incubated for 30 min prior to initiation of fibrillogenesis by addition of soluble IAPP. If seed activation is a required step, the lag phase should be diminished by this incubation. Under these conditions, the lag phase is, in fact, somewhat longer (Figure 4, curve C). An inflection point remains, but t_{50} grows to 1270 ± 90 s from 710 ± 30 s for cases in which the seed and soluble IAPP are added simultaneously. As the shape of the kinetic profile changes little, seed activation is unlikely to play a significant part in fibrillogenesis.

Last, consider the possibility that exogenous seed leads to the formation of new fibers. This was explored by varying the concentration of seed used in these reactions. If new fiber ends are not produced during growth, the rate law described previously, k[soluble IAPP][fiber ends], will hold, and reaction velocities of seeded reactions should vary linearly with initial seed concentrations. Seeded reactions were performed at 20 μM soluble IAPP in the presence of 0.5−2 μM seed (Figure 6A). Remarkably, over this range of seed concentrations, the $\nu_{t_{50}}$ of these reactions varies by a factor of ∼1.5, substantially less than the factor of 4 predicted by the previous rate law. Seeding with 0.5 μM standard seed gives a $\nu_{t_{50}}$ of 24 ± 4 nM/s, while seeding with 2 μM standard seed gives a $\nu_{t_{50}}$ of 36 ± 2 nM/s (Figure 6C). The characteristic time, t_{50}, was found to decrease with increasing seed concentrations (Figure 6B), 360 ± 40 s for 2 μM and 880 ± 30 s for 0.5 μM seed. Under these reaction conditions, this may be explained, in part, by the existence of a pre-elongation step on the timescale of the reaction (Figure 4).

The stability, structure, and reaction pathways of folding intermediates are readily explored by monitoring the dependence of kinetics on denaturant concentration (*26*, *27*). Using a standard reaction condition of 10 μM soluble IAPP, *de novo* reaction kinetics were determined at HFIP concentrations ranging from 2% to 4% (v/v). Surprisingly, these subtle

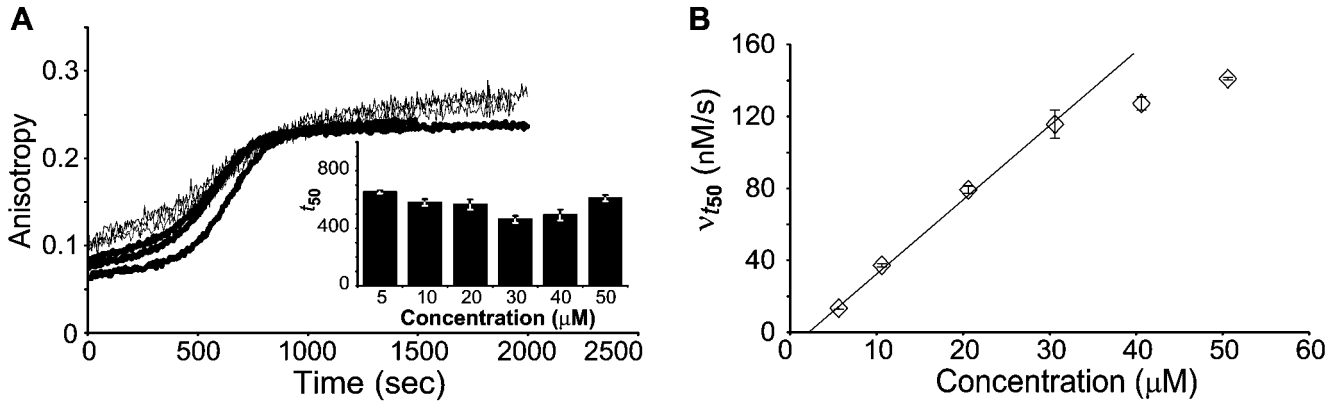

FIGURE 5: Effects of protein concentration on seeded IAPP fibrillogenesis reactions. (A) Representative kinetic profiles for seeded fiber formation reactions at initial IAPP concentrations of 5 μM (thin lines) and 50 μM (thick lines), seeded with 1 μM of standard seed. (A, inset) Average values of t_{50} for seeded fiber formation at initial IAPP concentrations of 5−50 μM. A linear fit ($R^2 = 0.99$) to protein concentrations through 30 μM is shown. (B) Reaction turnover, $\nu_{t_{50}}$, as a function of initial protein concentration. Error bars are ± SEM for three trials. The initial anisotropy of the 5 μM samples is larger than that of the 50 μM samples because of the larger relative contribution of the 1 μM of seed to the observed 5 μM anisotropy.

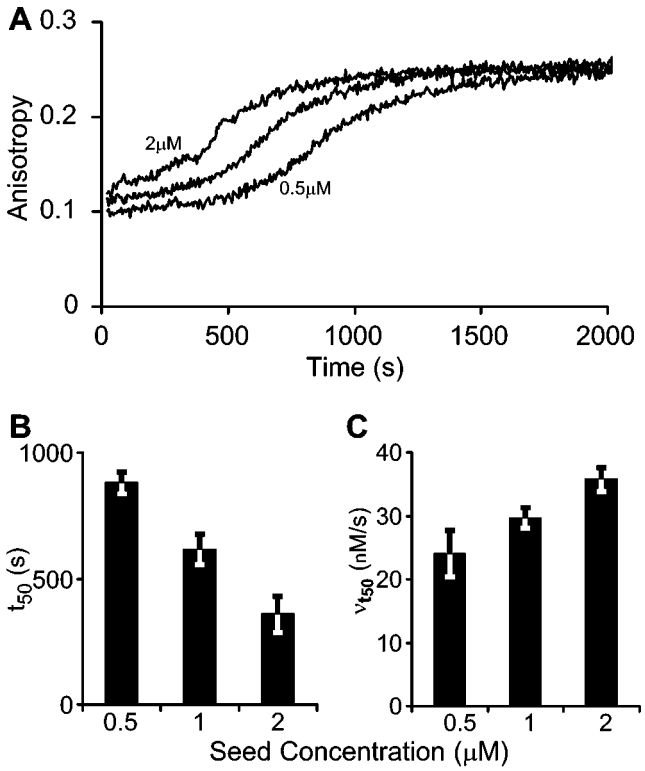

FIGURE 6: Effect of seed concentration on IAPP fibrillogenesis. Seed is added to a final concentration of 0.5−2 μM (monomer units) to a reaction containing 20 μM IAPP. (A) Representative kinetic profiles at 2, 1, and 0.5 μM are shown. (B) Average value of t_{50} as a function of seed concentration. (C) Average value of $\nu_{t_{50}}$ as a function of seed concentration.

variations in HFIP concentration had a striking impact on the fibrillogenesis kinetics (Figure 7A). The lag times for this reaction decrease ~35-fold when HFIP is increased from 2% to 4%, with $t_{50} = 250 \pm 50$ s at 4% HFIP and $t_{50} = 8600 \pm 1400$ s at 2% HFIP (Figure 7C). Similarly, $\nu_{t_{50}}$ increases by a factor of ~28 over the same range (Figure 7D), from 1.0 ± 0.02 nM/s at 2% HFIP to 28 ± 1 nM/s at 4% HFIP.

The decrease in t_{50} with increasing concentrations of HFIP fits well to a log−linear relationship between HFIP and t_{50} (Figure 7C). This is analogous to the slowing of protein folding kinetics by other denaturants (*28*) and the acceleration of folding by TFE (*26*). This suggests that the elements of the fibrillogenesis reaction which determine t_{50} are dominated by a single transition. The characteristic time, t_{50}, cannot be used to directly determine the transition energy for IAPP fiber formation; however, the slope of the plot may be related to the number of local hydrogen bonds involved in the final structure (*27*). Further, the close correlation of log(t_{50}) to HFIP concentration ($R^2 = 0.95$) permits extrapolation to 0% HFIP, giving a t_{50} of 2.8×10^5s or ~3.5 days.

To separate nucleation from elongation contributions, the dependence of seeded kinetics on HFIP concentration was also determined. Using otherwise identical conditions as the previous *de novo* studies, 10 μM soluble IAPP was reacted in the presence of 1 μM seed (Figure 7B). The most obvious consequence of higher concentrations of HFIP is the reduction of the lag phase evident in seeded reactions (Figure 4, curve A). This suggests that we have accelerated the pre-elongation step revealed by delayed introduction of seed (Figure 4, curve B). The dependence of t_{50} on HFIP concentration is smaller in seeded reactions than in *de novo* experiments. Average lag times for seeded reactions (Figure 7C) were $t_{50} = 970 \pm 80$ s at 2% HFIP and 110 ± 10 s at 4% HFIP. Similar to the *de novo* kinetics, the t_{50} of the seeded kinetics fit well to a log−linear relationship. The slopes of the fit is -1.3 (% HFIP)$^{-1}$, which is comparable to the slope of -1.8 (% HFIP)$^{-1}$ for the *de novo* reactions. Consistent with the idea that HFIP impacts seeded reactions most by accelerating the pre-elongation step, $\nu_{t_{50}}$ increases only marginally (Figure 7C) from 12 ± 2 nM/s at 2% HFIP to 47 ± 8 nM/s at 4% HFIP. At 4% HFIP, the increase in $\nu_{t_{50}}$ and the decrease in t_{50} is due, in part, to *de novo* fiber formation. *De novo* fiber formation at 4% HFIP has a $t_{50} = 250 \pm 50$ s, which is comparable to the $t_{50} = 110 \pm 10$ s of the seeded reaction.

DISCUSSION

Determination of the mechanism of IAPP fiber formation is a critical step in explaining IAPP's role in type II diabetes pathology. Here, we perform several experiments aimed at elucidating the basic *in vitro* assembly steps of IAPP fibers. We observe five behaviors in the kinetics of IAPP fibrillo-

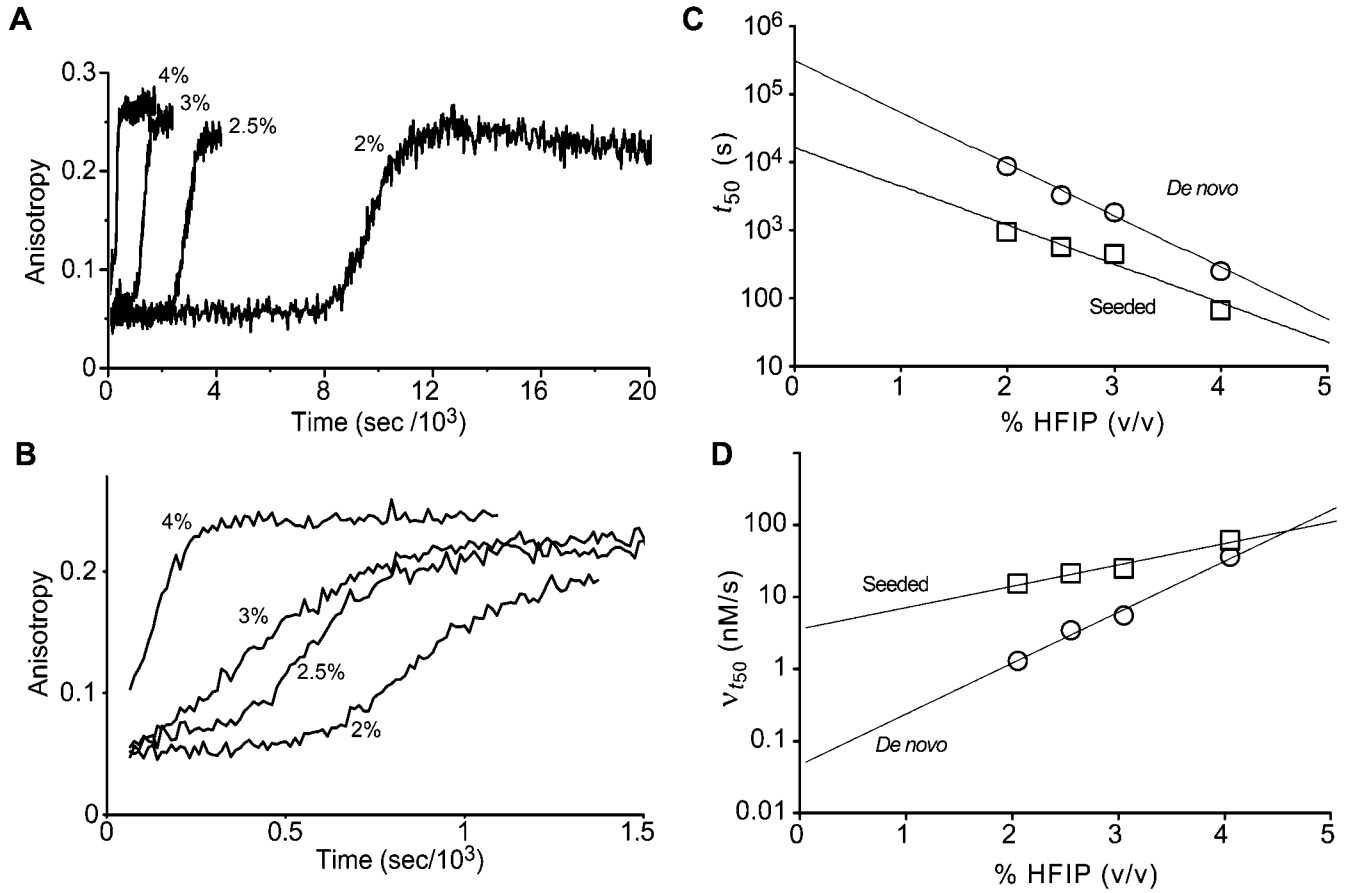

FIGURE 7: Effect of HFIP on the fiber formation kinetics of IAPP. (A) Representative kinetic profiles of 10 μM IAPP *de novo* fiber formation reactions at 2−4% (v/v) HFIP. (B) Representative kinetic profiles from 10 μM IAPP precursor seeded with 1 μM seed at 2−4% HFIP. (C and D) Log−linear plots of average values of t_{50} and $\nu_{t_{50}}$ from triplicate experiments. Both *de novo* (open squares) and seeded (open circles) reactions are shown. Linear fits are shown, $R^2 \geq 0.94$ in all cases. Error bars are not shown, as they are maximally the same size as the symbol. Note, for seeded reactions as a function of HFIP (B), the values of $\nu_{t_{50}}$ were measured from the slope at the anisotropy value of 0.15. Similarly, the t_{50} were calculated from the time to reach an anisotropy of 0.15.

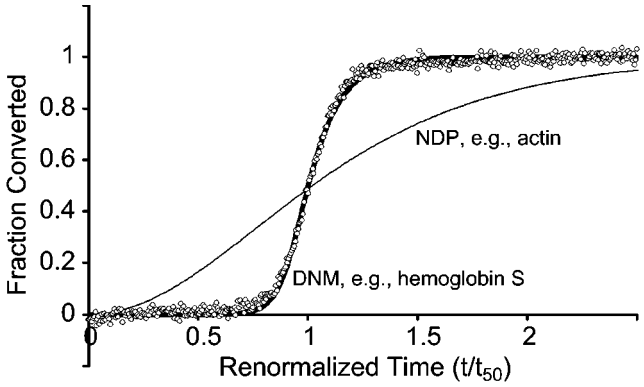

FIGURE 8: Comparison of IAPP kinetic profiles to fundamental protein polymerization models. The IAPP data set (open circles, *de novo* reaction at 30 μM IAPP) is clearly more similar in shape to DNM kinetics (thick line) than to NDP kinetics (thin line). DNM parameters were chosen to match the kinetic profile of IAPP kinetics. On time and intensity renormalized axes, NDP parameters have little effect on the shape of their kinetic profile (*19*). All curves have been intensity renormalized (final value = 100% fiber; initial value is 0% fiber) and time renormalized relative to t_{50}.

genesis. (i) *De novo* fiber growth occurs suddenly; the time required for fiber growth, measured by the time for 20−80% of conversion to occur, is less than one-quarter of the half-time, t_{50}. (ii) Fibrillogenesis can be seeded (i.e., the t_{50} is reduced by adding a small amount of preformed fiber). (iii) The seeded kinetic profile shows an inflection point, which disappears if a delay is added between the preparation of a *de novo* reaction and the addition of seed. (iv) The kinetic profiles of *de novo* and seeded fibrillogenesis are independent of IAPP concentration. (v) The concentration of the cosolvent HFIP has a dramatic affect on the timescale of fibrillogenesis.

Fibrillogenesis Mediated by Two Nucleation Steps. Theories of protein polymerization have existed for decades and serve as the starting point for our analysis of fibrillogenesis kinetics. The canonical model of protein polymerization is the nucleation-dependent polymerization (NDP) model developed for actin (*25*). The NDP kinetic model consists of three steps: (i) monomer rapidly assembles into a range of high-energy oligomers, (ii) oligomers of sufficient size slowly convert to fiber nucleus (primary nucleation), and (iii) monomers elongate fibers by addition to the ends of fibers. The population of oligomers that convert to nucleus scales with the total concentration raised to the power of the oligomeric size. As the primary nucleation rate is dependent on this concentration of oligomers, the nucleation rate and many properties of the system show a very high concentration dependence. NDP describes the kinetic profiles (Figure 8), seeding capability (the addition of exogenous nuclei), and strong concentration dependence of actin polymerization (*25*).

The NDP model does not explain all protein fibrillogenesis reactions that show a similar overall concentration dependence. The timescale of hemoglobin S (HbS) polymerization shows a high-order (roughly 30th) dependence on HbS concentration. This initially suggested that a process similar to NDP was the polymerization mechanism (*29*). It was later observed that the kinetic profile of HbS polymerization demonstrated a much sharper transition than could be accounted for by the NDP model (*30*). This observation necessitates a nucleation rate which increases with time, a phenomenon readily explained by a double-nucleation mechanism (DNM) (*20*). The DNM model, similar to NDP, includes primary nucleation (i.e., production of fiber ends from bulk solution) and elongation of those ends. Further, the DNM model adds a second nucleation step which is fiber-dependent. This secondary nucleation contributes little to the total nucleation rate when little fiber is present and dominates the nucleation rate when large quantities of fiber are present (i.e., near t_{50}). This results in an accelerating conversion rate as fiber is produced. There are many possible mechanisms by which secondary nucleation may occur. For example, in HbS, it is by templated nucleation using a nongrowing surface of a fiber (*20*). On a time axis renormalized plot, NDP and DNM kinetic profiles are readily distinguished (Figure 8). A parabola closely approximates the early portions of the NDP curve. This is explained by a nearly constant nucleation rate over this range. By contrast, the DNM curve is quite flat initially, with no apparent polymer formation, and then the entire population is rapidly converted.

IAPP polymerization kinetics show a profile necessitating the presence of a secondary nucleation process (Figure 8). On a time axis and intensity renormalized plot, simulated NDP kinetic profiles are insensitive to the choice of parameters for the simulation (*19*). All NDP kinetic profiles show an inflection point (change from positive curvature to negative curvature) but never show a flat lag phase. By $t = t_{50}/2$, for the NDP model, significantly more than 10% of the total change has already occurred. By contrast, *de novo* IAPP polymerization is undetectable at $t = t_{50}/2$ (Figure 8). As with HbS, our explanation of this behavior is a second fiber-dependent means of generating fiber ends, which dominates as soon a small quantity of fiber is produced (*20*). Given the similarity of DNM kinetic profiles to IAPP polymerization kinetic profiles (Figure 8), we infer that IAPP polymerization proceeds with two kinetically significant nucleation steps, which we term primary and secondary nucleation.

Reaction Order During the Lag Phase. The concentration dependence of *de novo* polymerization reactions is the primary tool for elucidating the parameters describing nucleation and elongation in DNM kinetics. In this regard, IAPP differs sharply from HbS, as the *de novo* reaction lag phase is concentration-independent and should have minimally scaled with the square root of IAPP concentration (i.e., $10^{1/2}$ or ~3-fold) (Figure 3A). Indeed, in the case of HbS, the lag phase scales by the 30th power of protein concentration (*29*). Furthermore, the transition time for IAPP polymerization (time between 20% and 80% conversion) is also concentration-independent. When fibrillogenesis reactions at 5 and 50 μM are compared, we find the transition time to be roughly equal. As there is 10-fold more peptide to be converted at 50 μM than at 5 μM, this means that the rate at which fiber is converted has increased by 10-fold. Indeed, $\nu_{t_{50}}$ increases linearly with concentration and, under DNM, should have scaled minimally with the square of protein concentration (Figure 3B).

A critical event in DNM kinetics is the time point at which secondary nucleation outpaces primary nucleation, $t = t^*$. As secondary nucleation is dependent on the concentration of fiber, this will be a time point near the onset of detectable fiber formation. Kinetic profiles are the same for all of the *de novo* kinetics, implying that t^* is proportional to t_{50}. Adding seed to a fiber formation reaction bypasses the lag phase and skips to a condition similar to a *de novo* reaction time between t^* and t_{50}. Seeding a range of IAPP concentrations with a constant quantity of fiber results in values of t_{50} that do not change appreciably (Figure 5A, inset). By contrast, seeding a constant concentration of precursor IAPP with different quantities of fiber results in measurable changes to t_{50} and $\nu_{t_{50}}$ (Figure 6). The latter reaction shows that kinetics are perturbed by the amount of fiber present, while the former shows that, for a fixed amount of fiber, kinetics are invariant with concentration. Therefore, the concentration independence of *de novo* reactions suggests that, during the lag phase, $t < t^*$, a fixed quantity of fiber is produced. This requires that primary nucleation, secondary nucleation and elongation to be concentration-independent during the time leading up to t^*. The interactions leading to fiber formation are therefore fundamentally different from the single-phase diffusion-limited interactions typically invoked for generalized DNM fibrillogenesis reactions.

Requirement of a Phase Transition. Nucleation and elongation processes must behave in an IAPP concentration-independent manner during the lag phase. The system must also behave in a linearly concentration-dependent manner during the growth phase. However, oligomerization events are necessarily dependent on at least the square of protein concentration. These behaviors can be explained by invoking a single phenomenon. An apparent concentration independence may be generated if IAPP partitions into two populations: a soluble population that participates in nucleation and elongation and a reservoir population that keeps the soluble phase at a constant concentration. If amyloid assembly draws only on the soluble pool of IAPP monomer and the concentration of soluble IAPP is mediated by a solubility limit, termed c^*, then the system will behave in a concentration-independent manner during the lag phase. Below c^*, the length of the lag phase will cease to be concentration-independent and should reveal information about the underlying concentration dependence of the nucleation processes. Our data suggests that c^* is well below 5 μM IAPP and, therefore, may not be directly observable by tyrosine fluorescence anisotropy.

A reservoir phase also allows us to explain the concentration dependence of the growth phase. If the system continued to behave as concentration independent throughout the growth phase, the growth phase length would scale directly with the total concentration. Instead, it is the maximum rate of elongation, $\nu_{t_{50}}$, which scales linearly with total concentration (Figure 3B), suggesting first-order dependence on total IAPP concentration during the growth phase. As the rate of precursor consumption increases by many orders of magnitude over the course of the fibrillogenesis reaction, the rate at which the reservoir phase replenishes the soluble IAPP

likely becomes rate-limiting. We conjecture that the reservoir phase is a dispersion (i.e., a finely divided phase which does not readily separate from the bulk solution) with a characteristic size distribution. In such a case, the rate of release of soluble IAPP will scale in direct proportion to the mass of the dispersed phase. Thus, invoking a dispersed reservoir phase allows the system to simultaneously behave in a fashion independent of total IAPP concentration during the lag phase and linearly dependent on IAPP concentration during the growth phase. This explains both the concentration independence of t_{50} and the first order dependence of $\nu_{t_{50}}$ on IAPP concentration.

Activation of IAPP. Seeded kinetic profiles in DNM kinetics are typically anticipated to follow an exponential decay. IAPP's seeded kinetic profiles all show an inflection point (Figures 2, 5A, and 6A). An inflection point in a seeded kinetic might be explained if soluble IAPP undergoes a conformational change that occurs slowly and confers on IAPP the ability to elongate existing fibers. Such a change is demonstrated by the disappearance of the inflection point upon adding seed 20−30 min after preparation of the IAPP solution (Figure 4). A conformational change prior to participation in fibrillogenesis processes was observed in actin polymerization. This change, referred to as monomer activation, was explained by the exchange of Ca^{2+} for Mg^{2+}, which then accelerates fiber nucleation (*18*, *31*). The origin of a conformational change in IAPP is unclear. It may be an intrinsic property of the monomeric peptide or an event coupled to the release of peptide from the reservoir phase. As the inflection point in seeded kinetics disappears before growth is measurable in *de novo* kinetics, it is likely that activation dominates elongation and not nucleation processes.

Perturbation of Secondary Structure and Solubility. The fluorinated alcohol HFIP accelerates both *de novo* and seeded IAPP fibrillogenesis. This may act by increasing the concentration of soluble IAPP. As the primary and secondary nucleation rates should depend on the concentration of soluble IAPP, perturbation of the dispersion concentration could have a dramatic impact on the length of the lag phase. An alternative explanation derives from the observation that fluorinated alcohols accelerate protein folding in a manner that correlates with the number of local hydrogen bonds (*27*). Because of this property we suggest that, at low concentration, HFIP accelerates polymerization through the stabilization of local hydrogen-bonded structure. Consistent with this, we observe the acceleration of fiber formation in IAPP preparations containing low percentages of TFE (data not shown). CD spectroscopy (Figure 1C) (*13*, *32*), Fourier transform infrared spectroscopy, and fiber diffraction (*33*) all suggest that IAPP fibers are predominantly β-sheet structures. Further, the presence of contact between residues 15, 23, and tyrosine 37 (*12*), a proposed 5 nm IAPP protofiber width (*21*) and the general instability of β strands longer than seven residues (*34*), all suggest that a turn is necessary in the structure. The necessity of a β turn suggests that HFIP acts by stabilizing an on-pathway but unstable β turn topology (*35*). HFIP's effect is ~7-fold greater in *de novo* reactions than in seeded reactions. As primary nucleation is bypassed in the latter, the former suggests that stabilized β turns serve a critical role in primary nucleation.

The impact of HFIP on the timescale of polymerization extrapolates to several days (Figure 7B) in the absence of HFIP. Previously reported values of t_{50} for IAPP fibrillogenesis span a range of up to several days (*13*, *32*). These studies do not, however, account for the residual organic solvent present in the reaction media. Furthermore, studies using DMSO as cosolvent require the presence of nonionic surfactants for fiber formation to take place on a laboratory timescale (*36*). We suggest, therefore, that the disparity in timescales reported for IAPP fibrillogenesis derives from changes in the solubility of free IAPP.

Dispersed Phase-Mediated Fibrillogenesis. We summarize these results in a model, dispersed phase-mediated fibrillogenesis (PMF). There are three ways fibrillogenesis is mediated in this model. First, activation is mediated by the formation and presence of a dispersed phase and subsequent release of a low concentration of soluble peptide. Second, nucleation processes are mediated by the constant monomer concentration to yield a concentration-independent lag phase. As nucleation proceeds, the elongation process accelerates, as a consequence of the increasing number of ends for elongation. Third, the elongation process becomes first-order when it reaches a sufficient rate to be limited by the breakdown of the dispersed reservoir phase to soluble monomer. When seeded, fiber production is limited immediately by the availability of activated, soluble IAPP. Further, as the population of fiber increases, secondary nucleation accelerates, and the reaction speeds up. Thus, the seeded kinetics are dominated by secondary nucleation and by activation processes.

A dispersed protein phase as proposed in the PMF model has been observed in the folding and aggregation pathways of other proteins. The tetramerization pathway of corticotropin-releasing factor is thought to have a peptide micelle as an intermediate (*37*). At low pH, Aβ_{1-40} polymerization shows light scattering evidence for aggregates roughly 7 nm in size (*38*). Further, an oligomeric reservoir phase may also explain the nature of a now frequently observed intermediate in amyloid fiber formation. Spherical structures, detected via AFM or TEM, have been observed prior to fiber formation in Aβ_{1-40}, Aβ_{1-42} (*39*, *40*), α-synuclein (*41*), and more recently the NM domain of the yeast prion Sup35 (NM) (*42*). IAPP itself has been reported to form an amorphous aggregate prior to fiber formation (*32*). Prevalence of a dispersed phase in amyloid kinetic pathways may explain why few amyloid proteins have shown the concentration dependence expected from generalized DNM kinetics. For example, neither Aβ (*38*, *43*) nor NM (*42*) show a strong dependence of kinetic timescales on protein concentration. Interestingly, NM also shows an inflection point in its seeding kinetics, when seeded with low concentrations of unsonicated seed (*44*). The fibrillogenesis model proposed for NM, nucleated conformational conversion (NCC) (*42*), contains a step similar to the dispersed phase formation proposed here. The role of these aggregates in fibrillogenesis is, however, distinct from the dispersed phase proposed in PMF. In NCC, the spherical intermediates participate directly in both nucleation and elongation processes, while, in PMF, the intermediate is an off-pathway phase. Nevertheless, the overall similarity of the two approaches, specifically the inclusion of partitioning into phases with distinct behaviors in fibrillogenesis, suggests that dispersed reservoir phases are widely applicable to amyloid fibrillogenesis.

The kinetic behavior described here gives insight into the mechanism of amyloid deposition *in vivo*. Pancreatic amyloid formation forms slowly in the intercellular space surrounding the islet β cells in patients with type II diabetes. Type II diabetics develop resistance to insulin, and as a result, turnover IAPP containing insulin granules more frequently. This has been suggested to elevate the IAPP above the critical concentration for nucleation-dependent polymerization and lead to amyloid deposition. The conclusion drawn from this study is that amyloid formation is unlikely to occur because of a transient IAPP concentration increase around the islet β cells. The high concentration of IAPP in the granules themselves argues that concentration variation is an unlikely cause of *in vivo* IAPP amyloid formation. We suggest that, in the body, some other factor, analogous to HFIP or Triton X-100, such as a perturbed membrane environment or serum lipid composition in obese patients, may enhance nucleation. Importantly, the PMF model can serve as a framework for testing the effects of additives on specific elements of the fibrillogenesis pathway. This will facilitate the search for agents that trigger fiber formation *in vitro* and ligands which may inhibit amyloid deposition *in vivo*.

ACKNOWLEDGMENT

We thank Dr E. M. De La Cruz, J. Larson, Dr S. Jaswal, and Dr T. D. Pollard for helpful discussions and critical reading of this manuscript. We thank Dr. Vincenz Unger for use and assistance with electron microscopy.

REFERENCES

1. Rochet, J. C., and Lansbury, P. T., Jr. (2000) *Curr. Opin. Struct. Biol. 10*, 60−68.
2. Floege, J., and Ketteler, M. (2001) *Kidney Int. 59* (Suppl. 78), S164−S171.
3. Hoppener, J. W., Ahren, B., and Lips, C. J. (2000) *N. Engl. J. Med. 343*, 411−419.
4. Kahn, S. E., Andrikopoulos, S., and Verchere, C. B. (1999) *Diabetes 48*, 241−253.
5. Sunde, M., Serpell, L. C., Bartlam, M., Fraser, P. E., Pepys, M. B., and Blake, C. C. F. (1997) *J. Mol. Biol. 273*, 729−739.
6. Harper, J. D., and Lansbury, P. T., Jr. (1997) *Annu. Rev. Biochem. 66*, 385−407.
7. Esler, W. P., Stimson, E. R., Fishman, J. B., Ghilardi, J. R., Vinters, H. V., Mantyh, P. W., and Maggio, J. E. (1999) *Biopolymers 49*, 505−514.
8. Chien, P., and Weissman, J. S. (2001) *Nature 410*, 223−227.
9. Lorenzo, A., Razzaboni, B., Weir, G. C., and Yankner, B. A. (1994) *Nature 368*, 756−760.
10. Kahn, S. E., D'Alessio, D. A., Schwartz, M. W., Fujimoto, W. Y., Ensinck, J. W., Taborsky, G. J., Jr., and Porte, D., Jr. (1990) *Diabetes 39*, 634−638.
11. Hutton, J. C. (1989) *Diabetologia 32*, 271−281.
12. Padrick, S. B., and Miranker, A. D. (2001) *J. Mol. Biol. 308*, 783−794.
13. Kayed, R., Bernhagen, J., Greenfield, N., Sweimeh, K., Brunner, H., Voelter, W., and Kapurniotu, A. (1999) *J. Mol. Biol. 287*, 781−796.
14. Westermark, P., Engstrom, U., Johnson, K. H., Westermark, G. T., and Betsholtz, C. (1990) *Proc. Natl. Acad. Sci. U.S.A. 87*, 5036−5040.
15. LeVine, H., III (1999) *Methods Enzymol. 309*, 274−284.
16. Lakowicz, J. R. (1999) *Principles of Fluorescence Spectroscopy*, 2nd ed., Kluwer Academic/Plenum Publishers, New York.
17. Barshop, B. A., Wrenn, R. F., and Frieden, C. (1983) *Anal. Biochem. 130*, 134−145.
18. Cooper, J. A., Buhle, E. L., Jr., Walker, S. B., Tsong, T. Y., and Pollard, T. D. (1983) *Biochemistry 22*, 2193−2202.
19. Ferrone, F. (1999) *Methods Enzymol. 309*, 256−274.
20. Ferrone, F. A., Hofrichter, J., and Eaton, W. A. (1985) *J. Mol. Biol. 183*, 611−631.
21. Goldsbury, C. S., Cooper, G. J. S., Goldie, K. N., Muller, S. A., Saafi, E. L., Gruijters, W. T. M., and Misur, M. P. (1997) *J. Struct. Biol. 119*, 17−27.
22. Jarrett, J. T., and Lansbury, P. T., Jr. (1993) *Cell 73*, 1055−1058.
23. Bolen, D. W., and Santoro, M. M. (1988) *Biochemistry 27*, 8069−8074.
24. Larson, J. L., Ko, E., and Miranker, A. D. (2000) *Protein Sci. 9*, 427−431.
25. Oosawa, F., and Asakura, S. (1975) *Thermodynamics of the polymerization of protein*, Academic Press, New York.
26. Buck, M. (1998) *Q. Rev. Biophys. 31*, 297−355.
27. Hamada, D., Chiti, F., Guijarro, J. I., Kataoka, M., Taddei, N., and Dobson, C. M. (2000) *Nat. Struct. Biol. 7*, 58−61.
28. Jackson, S. E. (1998) *Folding Des. 3*, R81−R91.
29. Hofrichter, J., Ross, P. D., and Eaton, W. A. (1974) *Proc. Natl. Acad. Sci. U.S.A. 71*, 4864−4868.
30. Eaton, W. A., and Hofrichter, J. (1978) in *Biochemical and clinical aspects of hemoglobin abnormalities* (Caughey, W. S., and Caughey, H., Eds.), pp 443−457, Academic Press, New York.
31. Frieden, C. (1983) *Proc. Natl. Acad. Sci. U.S.A. 80*, 6513−6517.
32. Higham, C. E., Jaikaran, E. T., Fraser, P. E., Gross, M., and Clark, A. (2000) *FEBS Lett. 470*, 55−60.
33. Jaikaran, E. T., Higham, C. E., Serpell, L. C., Zurdo, J., Gross, M., Clark, A., and Fraser, P. E. (2001) *J. Mol. Biol. 308*, 515−525.
34. Stanger, H. E., Syud, F. A., Espinosa, J. F., Giriat, I., Muir, T., and Gellman, S. H. (2001) *Proc. Natl. Acad. Sci. U.S.A. 98*, 12015−12020.
35. Ramirez-Alvarado, M., Blanco, F. J., Niemann, H., and Serrano, L. (1997) *J. Mol. Biol. 273*, 898−912.
36. Kudva, Y. C., Mueske, C., Butler, P. C., and Eberhardt, N. L. (1998) *Biochem. J. 331*, 809−813.
37. Morii, H., Uedaira, H., Ishimura, M., Kidokoro, S., Kokubu, T., and Ohashi, S. (1997) *Biochemistry 36*, 15538−15545.
38. Lomakin, A., Chung, D. S., Benedek, G. B., Kirschner, D. A., and Teplow, D. B. (1996) *Proc. Natl. Acad. Sci. U.S.A. 93*, 1125−1129.
39. Huang, T. H., Yang, D. S., Plaskos, N. P., Go, S., Yip, C. M., Fraser, P. E., and Chakrabartty, A. (2000) *J. Mol. Biol. 297*, 73−87.
40. Harper, J. D., Wong, S. S., Lieber, C. M., and Lansbury, P. T., Jr. (1999) *Biochemistry 38*, 8972−8980.
41. Conway, K. A., Lee, S. J., Rochet, J. C., Ding, T. T., Williamson, R. E., and Lansbury, P. T., Jr. (2000) *Proc. Natl. Acad. Sci. U.S.A. 97*, 571−576.
42. Serio, T. R., Cashikar, A. G., Kowal, A. S., Sawicki, G. J., Moslehi, J. J., Serpell, L., Arnsdorf, M. F., and Lindquist, S. L. (2000) *Science 289*, 1317−1321.
43. Hasegawa, K., Yamaguchi, I., Omata, S., Gejyo, F., and Naiki, H. (1999) *Biochemistry 38*, 15514−15521.
44. Santoso, A., Chien, P., Osherovich, L. Z., and Weissman, J. S. (2000) *Cell 100*, 277−288.

BI0160462